

# Predicting Energy Budgets in Droplet Dynamics: A Recurrent Neural Network Approach

Diego A. de Aguiar <sup>\*1</sup>, Hugo L. França <sup>†2</sup>, and Cassio M. Oishi<sup>‡1</sup>

<sup>1</sup> *Departamento de Matemática e Computação, Faculdade de Ciências e Tecnologia, Universidade Estadual Paulista “Júlio de Mesquita Filho”, Presidente Prudente, Brazil*

<sup>2</sup> *Van der Waals-Zeeman Institute, Institute of Physics, University of Amsterdam, Amsterdam, The Netherlands*

Neural networks in fluid mechanics offer an efficient approach for exploring complex flows, including multiphase and free surface flows. The recurrent neural network, particularly the Long Short-Term Memory (LSTM) model, proves attractive for learning mappings from transient inputs to dynamic outputs. This study applies LSTM to predict transient and static outputs for fluid flows under surface tension effects. Specifically, we explore two distinct droplet dynamic scenarios: droplets with diverse initial shapes impacting with solid surfaces, as well as the coalescence of two droplets following collision. Using only dimensionless numbers and geometric time series data from numerical simulations, LSTM predicts the energy budget. The marker-and-cell front-tracking methodology combined with a marker-and-cell finite-difference strategy is adopted for simulating the droplet dynamics. In addition, as the code must handle various drop shapes, we have also employed a method designed for extracting particles from interfaces in digital images. Using a recurrent neural network (RNN) architecture fed with time series data derived from geometrical parameters, as for example droplet diameter variation, our study shows the accuracy of our approach in predicting energy budgets, as for instance the kinetic, dissipation, and surface energy trends, across a range of Reynolds and Weber numbers in droplet dynamic problems. Finally, a two-phase sequential neural network using only geometric data, which is readily available in experimental settings, is employed to predict the energies and then use them to estimate static parameters, such as the Reynolds and Weber numbers. While our methodology has been primarily validated with simulation data, its adaptability to experimental datasets is a promising avenue for future exploration. Finally, we hope that our strategy can be useful for diverse applications, spanning from inkjet printing to combustion engines, where the prediction of energy budgets or dissipation energies is crucial. This analysis provides insights for developing machine learning modeling using numerical and/or experimental data from droplet dynamics.

**keywords:** Droplets | Numerical solution | Prediction | Surface Tension | LSTM | Energy budget

## I. INTRODUCTION

Droplet dynamics, a phenomenon of remarkable complexity and practical significance, extends its influence across various domains of science and engineering, ranging from raindrop splashes on leaves to the precise deposition of microdroplets in advanced manufacturing processes. Achieving a fundamental understanding of the dynamics governing droplet impact represents a significant scientific challenge, needing the collaborative engagement of experimental, analytical and numerical methodologies. This concerted effort is essential to unravel the complexities inherent in the complex phenomenon of droplet impact dynamics.

Advancements in these methodologies have unveiled a wealth of intricate physical mechanisms governing liquid-drop impacts on rigid surfaces. These insights not only contribute to the fundamental understanding within the realm of fluid dynamics but also create innovations across a diverse array of applications. The implications of droplet impact dynamics reverberate through fields such as aerospace, energy, materials science, biotechnology, forensic analysis, and studies related to food and cosmetics, among others.

In recent decades, the exploration of the droplet dynamics has yielded a rich body of literature, including excellent review articles that provide comprehensive insights into the multifaceted aspects of

<sup>\*</sup>diego.aguiar@unesp.br, ORCID: 0000-0001-5159-867X

<sup>†</sup>franca.hugo1@gmail.com, ORCID: 0000-0002-5361-7704

<sup>‡</sup>cassio.oishi@unesp.br, ORCID: 0000-0002-5361-7704

droplet dynamics. Notable contributions in this context have been made, as well detailed in [1–4]. These articles clarify some important aspects as for instance: the dimensionless numbers and their influence on the maximum spreading of the droplet, different regimes considering pre- and post-impact and their consequences in terms of energy mechanisms, etc.

Concerning droplet dynamics and its applications, the complexities of the inkjet printing process stand out as a pertinent challenge. This process involves various fluid dynamics challenges that significantly impact the outcome of the printing process. A comprehensive overview of these challenges, particularly focusing on fundamental aspects, has been extensively discussed in the review paper by [5]. A fundamental question of inkjet printing challenge lies in the collision dynamics of droplets during their trajectory from ejection to eventual impact on the substrate. The understanding of this collision process is important, influencing the spatial distribution, size, and morphology of the printed droplets. As droplets traverse through the air, interactions can be observed, governed by fluid dynamics principles, as for instance coalescence, fragmentation, bouncing and other complex behaviors. After this, a different dynamic happens when the droplets impact on the substrate. Factors such as droplet velocity, angle of impact, and the properties of the drop and substrate all contribute to the final result. Moreover, the subsequent spreading of the droplets upon contact with the substrate adds another layer of complexity to the overall process. The dynamics of spreading govern how the ink interacts with the substrate surface, influencing factors as for instance the shape of the droplet. In essence, the challenges within inkjet printing underscore the profound interplay of fluid dynamics phenomena, encompassing droplet collisions, substrate interactions, and spreading dynamics. In this work, we have focused on two stages described in the review paper [5]: the impact of a droplet with different shapes in a substrate and the coalescence of droplets during the collision process.

Over the past decades, the simulation of droplet dynamics has been adopted for advancing our understanding of complex fluid phenomena [6]. These numerical investigations have opened new horizons, allowing for innovative approaches in the study of droplet behaviors and interactions. In these computational frameworks, the governing equations are rigorously solved on fixed or adaptive meshes, employing classical discretization schemes such as finite-element methods [7], finite volume methods [8], finite difference methods [9], among others. A critical computational consideration in simulating the impact and collisions of droplets is the treatment of the moving interface. This involves the solution of the adequate boundary conditions, coupled with the accurate representation and dynamic updating of the interface throughout the transient problem. Traditional mesh-based frameworks, commonly employed in the simulation of free surface or multiphase fluid flows, include the well-established front-tracking and front-capturing methodologies [10]. Beyond mesh-based approaches, mesh-free schemes have gained widespread application in simulating droplet dynamics. Smoothed Particle Hydrodynamics (SPH), for instance, offers an efficient and effective alternative of solving fluid dynamics problems without relying on a fixed grid allowing the solution of complex droplet interactions and deformations (see [11]). It is crucial to highlight the significance of both analytical papers within the context of impacting droplets [12] and experimental studies focusing on droplet dynamics [13]. These results play an important role in not only validating but also enriching the fidelity of computational simulations. Analytical works provide essential theoretical foundations, offering insightful equations and principles that guide numerical model development, as for instance the spreading of the droplet in a substrate [14]. Simultaneously, experimental investigations have been adopted to establish different scaling laws in the spreading of droplets [4, 15–19] and in droplet collisions [20–24]. The synergy between these analytical, experimental, and computational methods enhanced the understanding of droplet interactions [25–27].

More recently, the employment of Machine Learning (ML) strategies in the context of droplet dynamics received more attention due to the advances of new computation technologies, the increasing data availability and the implementation facilities on open-source codes (e.g. TensorFlow, Pytorch, MXNet, etc). The ML-based methods open a promising avenue to reduce both time and costs associated with traditional numerical simulations. This approach not only introduces efficiency gains but also serves as a robust alternative for predicting outcomes, reflecting the growing synergy between data-driven machine learning and traditional computational fluid dynamics. For example, in the context of droplet dynamics, different machine learning models have been adopted in order to predict physical or geometrical properties observed in complex flows, such as predicting the maximum spreading of a droplet by using the dimensionless numbers and properties related to each regime [28–33]. The idea of applying related features to predict fluid properties and/or characteristics was also explored by predicting drop morphologies adopting image data [34], classifying splashing and nonsplashing drops using images from when half of the drop impacted the surface [35], using an explainable artificial intelligence (XAI) to interpret how said classifier works and uncover a possible correlation between the spreading of a drop and the normalized impact force on a solid surface [36], predicting interface curvature through neighboring particles from 2D front-tracking representation [37], predicting size, velocity and shape characteristics of droplets from droplet-on-demand liquid metal jetting (DoD-LMJ) [38], etc.

The connection between droplet dynamics and the energy budget has been extensively documented. When a droplet approaches a surface or interacts with another droplet, it initiates a process of energy transfer involving kinetic, surface, and dissipative components. Examining the energy budget in droplet dynamics not only enhances our understanding of fundamental fluid dynamics principles but also facilitates the development of simple analytical models based on energy balance. For instance, expressions derived from energy conservation can be employed to construct equations predicting the maximum diameter of a droplet spreading on a rigid surface. Seminal works by [15], [39], [40] and [19] exemplify the application of such energy balance principles.

Exploring the energy budget in droplet dynamics is of practical significance, offering valuable insights for optimizing processes such as inkjet printing. Achieving precise control over droplet impact dynamics is crucial for obtaining desired outcomes in applications like these. Recent literature has presented several papers delving into the energy budget in complex droplet dynamics. For instance, in the context of impinging droplets on rigid surfaces, [41] utilized a Volume-of-Fluid code to investigate the effects of low and high velocities on surface energy and viscous dissipation. Simultaneously, [42] conducted an energy-budget analysis using the diffusive-interface method, with a focus on a two-dimensional case. Additional insights into the connection between splash formation and energy dissipation were provided by [43], who employed experimental results involving a ferrofluid droplet with various shapes. In droplet collision studies, [44] applied a front-tracking numerical scheme to study the energy budget using unequal-size droplets while [45] combined an energy-based strategy and binary droplet collisions through experimental setups to reanalyze the bouncing regime boundary on the regime map proposed by [22]. More recently, [46] explored the energy balance during coalescence and breakup after collision, utilizing an experimental process for droplet atomization. Additionally, [47] investigated electro-mechanical energy conversion in droplets.

Therefore, based on the literature review described in the previous statement, it is evident that numerous studies have focused on various aspects, such as the maximum spreading diameter, different scaling laws, and boundaries on the regime maps of droplet collisions, using arguments of energy conservation. However, these results are typically presented in the context of static analyses, as there are few works [41, 48] that deal with the transient variation of properties (such as the spreading of a droplet impacting a surface or the diameter and height of a coalesced drop after a drop-drop collision) and their relation to the transient energy budget. Notably, recent investigations using learning algorithms are also limited to static data analysis. In this work, we propose a machine learning model based on a recurrent neural network to predict the temporal variation of the energy budget. We have adopted the Long Short-Term Memory (LSTM) [49] with a geometric input data set  $z(t_1), \dots, z(t_n)$ , which learns a mapping to produce temporal predictions in terms of the energy budget. The term “geometric” refers to the time variation of the droplet diameter during spreading on a surface or the diameter and height of the coalesced droplet after the collision of two droplets. Expanding the potential of our framework utilizing LSTM, incorporating fluid parameters such as the Reynolds and Weber numbers, as well as flow parameters like impact parameter on the collision, enhances the accuracy of predictions for the transient behavior of kinetic, surface energies, and viscous dissipation. Although our tests have exclusively employed numerical results, the versatility of this non-intrusive methodology in predicting energy budgets during intricate droplet dynamics can be further extended to experimental investigations. This extension is feasible since it relies solely on temporal series data, specifically variations in droplet diameter, which can be easily captured by experimental devices.

## II. METHODS

### A. Mathematical model and overview of the numerical method

The equations that govern the flow behavior of isothermal and incompressible fluids are the continuity (1) and momentum (2) equations:

$$\nabla \cdot \mathbf{u} = 0, \quad (1)$$

$$\rho \left( \frac{\partial \mathbf{u}}{\partial t} + \nabla \cdot (\mathbf{u}\mathbf{u}) \right) = -\nabla p + \nabla \cdot \boldsymbol{\tau}, \quad (2)$$

where  $\mathbf{u}$  and  $p$  are the velocity and pressure fields and  $\rho$  is the fluid’s density. The stress tensor  $\boldsymbol{\tau}$  assumes a form of a Newtonian liquid as

$$\boldsymbol{\tau} = 2\eta\dot{\boldsymbol{\gamma}}, \quad (3)$$

where  $\eta$  is the viscosity of the fluid and  $\dot{\boldsymbol{\gamma}} = \frac{1}{2}(\nabla\mathbf{u} + (\nabla\mathbf{u})^T)$  is the strain-rate tensor with  $\nabla\mathbf{u}$  being the velocity gradient.

A dimensionless version of the previous equations can be obtained by scaling the variables as follows

$$\bar{\mathbf{x}} = \frac{\mathbf{x}}{D}, \quad \bar{t} = \frac{tU}{D}, \quad \bar{\mathbf{u}} = \frac{\mathbf{u}}{U}, \quad \bar{p} = \frac{p}{\rho U^2}, \quad \bar{\boldsymbol{\tau}} = \frac{D\boldsymbol{\tau}}{\eta U}, \quad (4)$$

using  $U$  and  $D$  as characteristic velocity and length, respectively. To simplify the nondimensionalization of the governing equations for isothermal and incompressible flows, we redefined them by using the previous dimensionless terms without its bars, as follows

$$\nabla \cdot \mathbf{u} = 0, \quad (5)$$

$$\frac{\partial \mathbf{u}}{\partial t} + \nabla \cdot (\mathbf{u}\mathbf{u}) = -\nabla p + \frac{1}{Re} \nabla^2 \mathbf{u}, \quad (6)$$

where  $Re = \frac{\rho U D}{\eta}$  is the dimensionless Reynolds number.

In our tests, there are two main boundary conditions to be considered: solid walls condition, to define behavior across domain boundaries, and the free surface condition, for the contact between fluid and the external environment (air). In summary, a no-slip condition is applied for solid wall contours, while the free surface condition is defined as

$$\begin{cases} \mathbf{n} \cdot (\mathbf{T} \cdot \mathbf{n}) = \gamma \kappa, \\ \mathbf{m} \cdot (\mathbf{T} \cdot \mathbf{n}) = 0, \end{cases} \quad (7)$$

where  $\mathbf{n}$  and  $\mathbf{m}$  are, respectively, the normal and tangential vectors to the free surface,  $\gamma$  is the surface tension coefficient,  $\kappa$  is the interface curvature and  $\mathbf{T} = \boldsymbol{\tau} - p\mathbf{I}$  is the total stress tensor. The nondimensionalized forms of (7) can be written as

$$\begin{cases} \mathbf{n} \cdot (\bar{\mathbf{T}} \cdot \mathbf{n}) = \frac{1}{We} \bar{\kappa}, \\ \mathbf{m} \cdot (\bar{\mathbf{T}} \cdot \mathbf{n}) = 0, \end{cases} \quad (8)$$

where  $\bar{\kappa} = D\kappa$ ,  $\bar{\mathbf{T}} = 2\bar{\boldsymbol{\gamma}} - Re \cdot \bar{p}\mathbf{I}$  and  $We = \frac{\rho U^2 D}{\gamma}$  is the Weber number. Furthermore, an extra dimensionless number is adopted for the collision regime, the impact parameter  $B = \frac{2b}{D_1 + D_2}$ , where  $b$  is the center-to-center relative distance between the drops and  $D_1, D_2$  are the diameters for each drop, as seen in [45].

To solve the governing equations numerically, we have employed the established projection method. In summary, the method uses the Helmholtz-Hodge decomposition to decouple velocity and pressure from equations (5) and (6). In the Helmholtz-Hodge decomposition, as presented in [50], any vector field defined in a region  $\Omega$  with smooth boundary  $\partial\Omega$  can be uniquely decomposed as

$$\tilde{\mathbf{u}} = \mathbf{u} + \nabla\psi, \quad (9)$$

where  $\mathbf{u}$  is a vector field such that  $\nabla \cdot \mathbf{u} = 0$  and  $\psi$  is a scalar field also defined in  $\Omega$ .

Initially, the projection method solves the momentum equation (6) for an intermediate velocity field  $\tilde{\mathbf{u}}$ . For the purpose of decoupling velocity and pressure, the unknown  $p$  is approximated by some known scalar field  $\tilde{p}$ , resulting in the following equation

$$\frac{\partial \tilde{\mathbf{u}}}{\partial t} + \nabla \cdot (\tilde{\mathbf{u}}\tilde{\mathbf{u}}) = -\nabla \tilde{p} + \frac{1}{Re} \nabla^2 \tilde{\mathbf{u}}, \quad (10)$$

with appropriated boundary conditions. After solving equation (10) and obtaining the velocity field  $\tilde{\mathbf{u}}$ , we still need to make sure the continuity equation will be satisfied. By using the Helmholtz-Hodge decomposition and equations (9) and (5), we can write the following Poisson equation for a scalar field  $\psi$

$$\nabla^2 \psi = \nabla \cdot \tilde{\mathbf{u}}. \quad (11)$$

Finally, by solving equations (10) and (11) we obtain  $\tilde{\mathbf{u}}$  and  $\psi$  so that the decomposition (9) can be used to obtain a final velocity field  $\mathbf{u}$  that satisfies both the momentum and continuity equations. The discretization process is achieved using the finite-difference method for free surface problems as well discussed in [51]. It is important to mention that we have employed an axisymmetric formulation to solve the droplet impacting problem, while droplet collision simulations were performed using a two-dimensional code.

## B. Energy budget

Since there will be no gravitational influence on the generated data, the energy budget is given by the kinetic energy, the surface energy and the viscous dissipation. The kinetic energy  $E_k$  is defined as

$$E_k = \int_V \frac{1}{2} \rho \|\mathbf{u}\|^2 dV, \quad (12)$$

calculated by the integral over the fluid volume  $V$ . Numerically, it is calculated as the sum of the kinetic energy inside all cells fully inside a droplet. The surface energy  $E_s$  is computed as

$$E_s = \int_S \gamma dS. \quad (13)$$

calculated by the integral over the fluid surface  $S$ . Lastly, based on the viscous dissipation, we can define

$$E_d = \int_t \int_V 2 \eta \|\dot{\gamma}\|^2 dV dt, \quad (14)$$

where  $\int_V 2 \eta \|\dot{\gamma}\|^2 dV$  is called the viscous dissipation rate.

The law of conservation of energy defines that the total sum of all the energies ( $E_t$ ) in the system must remain constant through time so that

$$E_t(t) = E_k(t) + E_s(t) + E_d(t) = E_t(0). \quad (15)$$

In order to construct a nondimensional investigation, we have adopted the following nondimensional energy quantities:

$$\begin{aligned} \bar{E}_k &= ReWe \int_{\bar{V}} \frac{1}{2} \|\bar{u}\|^2 d\bar{V}, \\ \bar{E}_s &= Re \int_{\bar{S}} 1 d\bar{S}, \\ \bar{E}_d &= We \int_{\bar{t}} \int_{\bar{V}} 2 \|\bar{\dot{\gamma}}\|^2 d\bar{V} d\bar{t}. \end{aligned}$$

The focus of this work is to use geometric time series data extracted from numerical simulations to generate time series predictions for each type of energy. From now on, we have omitted the bar over the nondimensional variables.

## C. Problem descriptions and data preparation

To apply the neural network solution, we first need to generate adequate datasets. In order to do so, numerical simulations are used to generate two different flow regimes: drop impact on a solid surface, to generate diverse spreading lengths with different initial drop shapes, and droplet collision, to test the capacity of the model to predict features that oscillate through time. Both problem descriptions are represented in Fig. 1 (left) while the schematic to obtain the dataset is also described in the same figure (right).

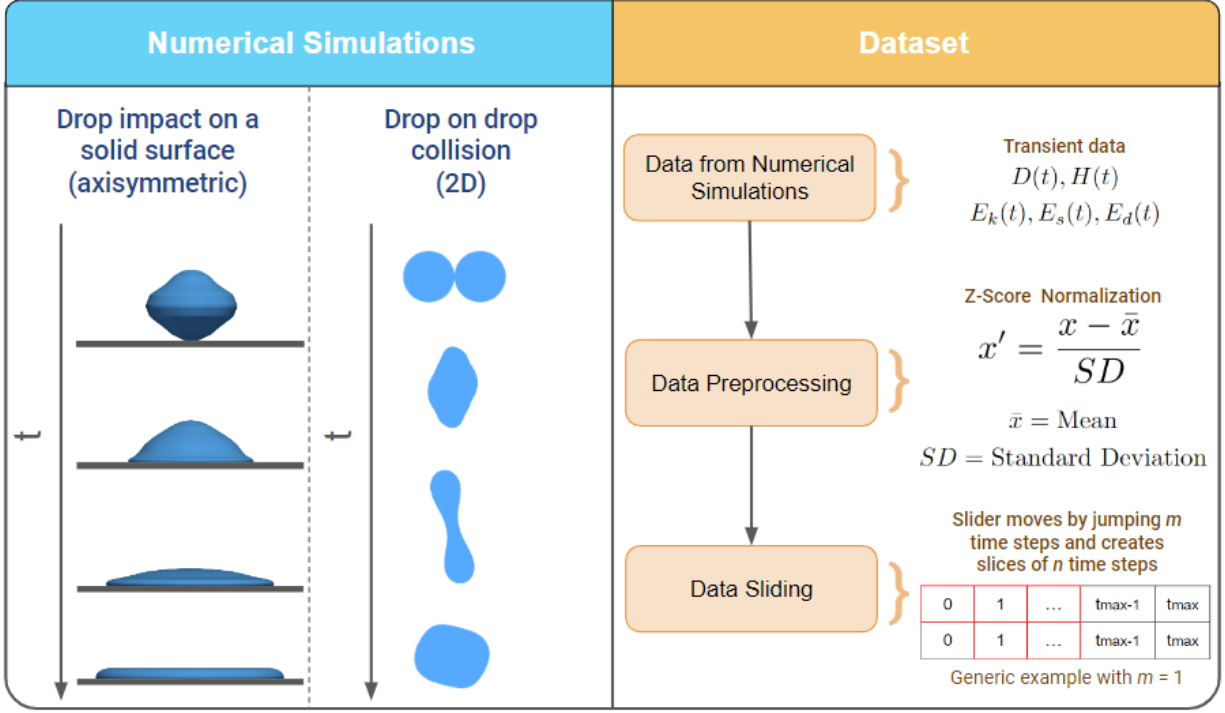


Fig. 1: Dataset is extracted from numerical simulations of two droplet dynamic problems.

In order to generate the dataset, each case is executed with varying fluid and flow parameters, and/or initial drop shapes. In the droplet impact scenario, we vary the droplet shape by extracting interfaces from experimental droplet images [43]. Conversely, for the droplet collision problem, we adopt the impact parameter  $B$  to induce variations. In both cases, modifications are also conducted changing the fluid parameters based on Reynolds and Weber numbers. In summary, samples within the dataset can be defined as individual data points, each characterized by a specific combination of features encompassing fluid and flow parameters as well as initial drop characteristics, as it will be detailed in the next sections.

### C.1 Spreading dataset

For the first dataset, we were inspired by the drop shapes from experiments presented by [43]. To test the efficiency of the machine learning model, the shapes were chosen in such a way that the train, validation and test subsets would have sufficiently different shapes, as shown in Fig. 2.

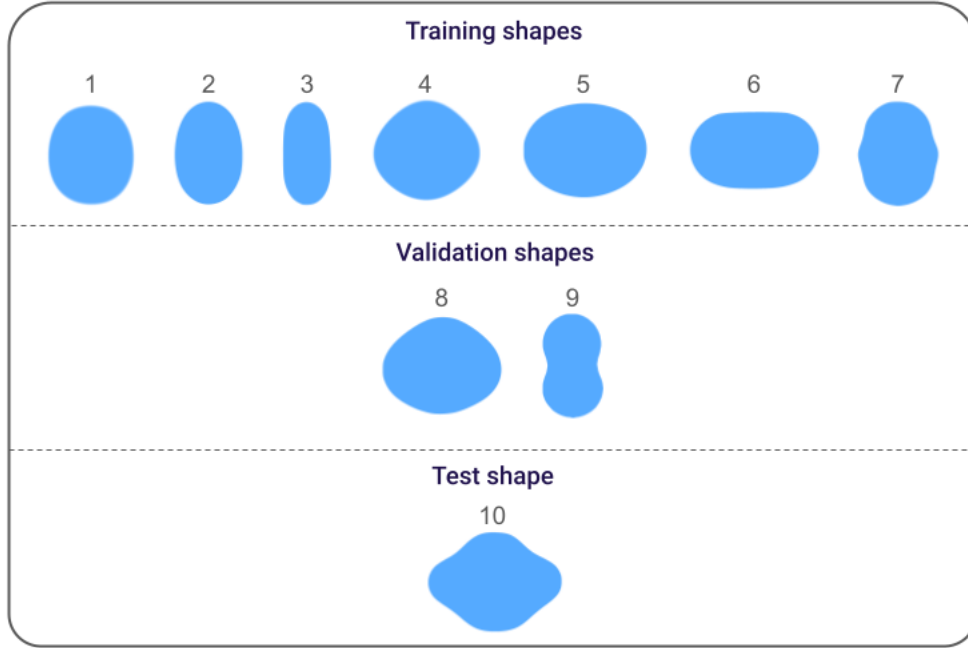


Fig. 2: Different initial drop shapes and the train-validation-test splits.

To extract particles from these shapes and simulate each case, an image interface extraction method was implemented, as described in Appendix A. The initial diameter and height of each shape, as presented in Table 1, are selected in such a way that each droplet has approximately the same volume. Since we used an axisymmetric simulation for the spreading case, as shown in Section A, this is necessary to make each droplet have approximately the same mass.

<i>Shape</i>	$D(0)$ (in mm)	$H(0)$ (in mm)
1	3.92	3.98
2	3.6771	4.64
3	2.62	4.64
4	4.64	3.6829
5	4.6086	3.1343
6	4.8143	2.5714
7	3.8229	4.24
8	4.5057	3.3857
9	3.5571	5.0086
10	4.6343	3.6229

Table 1: The initial spreading length and height for each drop shape.

The parameters chosen to configure the numerical simulations are presented in (Table 2). For each set of parameters and one droplet shape, a numerical simulation is run to generate one sample. Some combinations have fewer samples due to potential numerical errors in the solver, resulting in the failure to generate them. The Reynolds and Weber numbers were arbitrarily defined by varying the impact velocity. In total, 132 samples were extracted.

Spreading dataset		
<i>Samples</i>	Re	We
10	1.5063	240.625
10	4.5188	2165.625
10	5.875	212.5
10	10.2438	184.375
10	17.6250	1912.5
10	20.4375	118.75
10	24.8063	90.625
9	30.6313	53.125
10	30.7313	1659.375
7	35	25
10	61.3125	1068.75
9	74.4188	815.625
9	91.8938	478.125
8	105	225

Table 2: Number of samples for each group of parameters used in the spreading simulations.

To visualize the spreading behavior while varying Re and We, we have presented in Fig. 3 the droplet morphology and the temporal evolution of the diameter for shapes 1 and 10. As depicted in this figure, increasing the Reynolds number results in a greater spread for both shapes. This behavior is quantified by the subplots in Fig. 3 depicting the time variation of the droplet diameter. Figs. 3(a) and 3(b) illustrate snapshots comparing two shapes for two different sets of dimensionless numbers, while Figs. 3(c) and 3(d) compare the evolution of the spreading diameter through time for both shapes. It is evident from Figs. 3(a) and 3(c) that at lower Reynolds numbers, the droplets spread more slowly compared to the second test involving higher  $Re$ .

## C.2 Collision dataset

The second dataset consists of two drops of 1mm in diameter colliding horizontally with one another. The pair of drops merge after collision and generates horizontal and vertical oscillation over time, helping to create a time series that is harder to predict and that can be used to test the machine learning model’s efficiency.

To define the numerical simulation parameters for each sample, cases similar to those presented in the experimental coalescence map from [45] were selected by varying the impact velocity. For each set of Reynolds and Weber numbers, 20 simulations are run by varying the impact parameter B in the intervals shown in Table 3. Once again, certain samples were not successfully run due to solver errors. In total, 72 samples were generated.

Collision dataset			
<i>Samples</i>	Re	We	B (interval)
20	74.451	22.0	[0.0, 0.4]
20	85.4788	29.0	[0.0, 0.4]
9	97.8478	38.0	[0.0, 0.2316]
5	104.0863	43.0	[0.0211, 0.1684]
7	109.9715	48.0	[0.0421, 0.1684]
6	115.5573	53.0	[0.0421, 0.2105]
5	120.8853	58.0	[0.0, 0.2316]

Table 3: Number of samples for each group of parameters used in the collision simulations.

To visualize the difference in horizontal and vertical spreading after impact resulting from changes in the physical parameters and the impact parameter, snapshots from some simulated samples are shown in Fig. 4. Figs. 4(a), 4(b), and 4(c) illustrate snapshots of two coalescing droplets on three different sets of dimensionless numbers, with pairs 4(a) and 4(b) varying only the Reynolds and Weber numbers, and 4(a) and 4(c) varying only the impact parameter. For Figs. 4(d), 4(e), and 4(f), we compare the time series of diameter and height oscillation for each example.



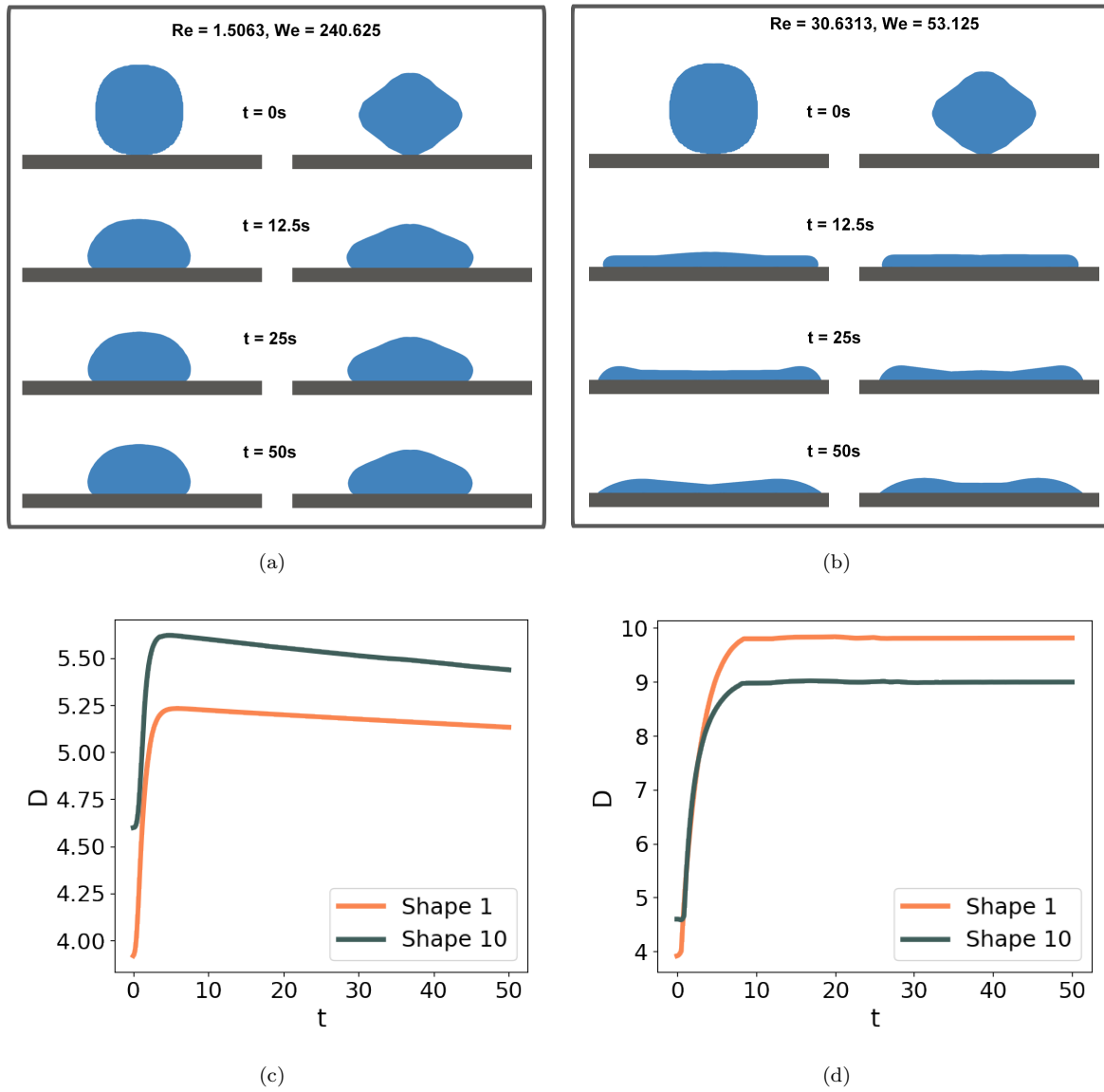


Fig. 3: Effect of drop shape (shapes 1 and 10 from Fig 2) on impact when varying  $Re$  and  $We$ : morphology for the first (a) and second (b) set of parameters and diameter time variation for both shapes from the first (c) and second set (d).

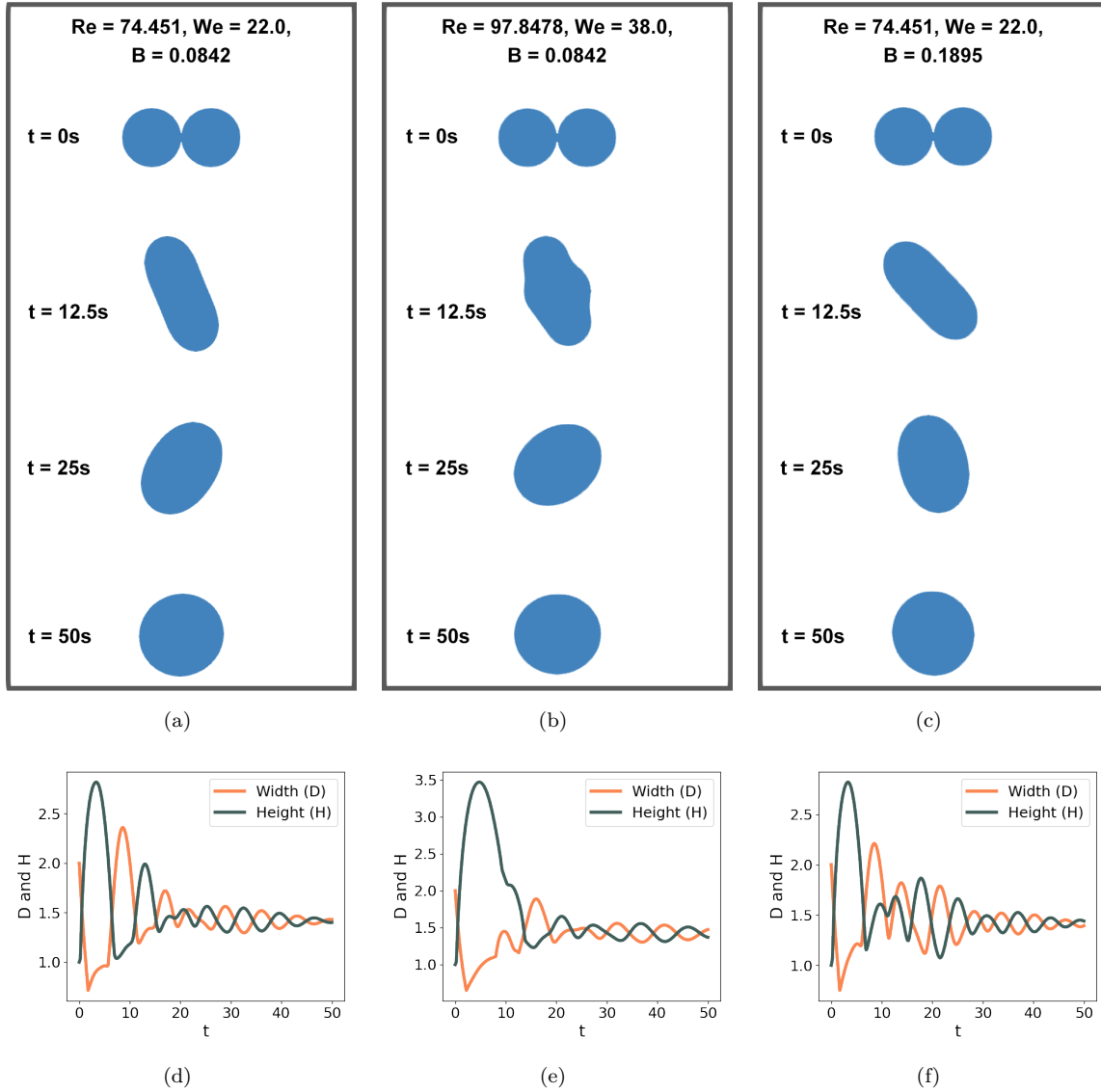


Fig. 4: Droplet collision dynamics with different impact parameters and varying  $Re$  and  $We$ : morphology for the first (a), second (b) and third (c) set of parameters and time variation in diameter  $D$  and height  $H$  for the first (d), second (e) and third set (f).

## D. Machine learning model

Since the transient features in the extracted data have a certain degree of time-correlation, it would be beneficial to use a neural network architecture that can capture it effectively. For this purpose, a Recurrent Neural Network [52], which can be used to find correlations on data sequences, is a good option.

The drawback of a simple RNN architecture is the likely introduction of the vanishing gradient problem [53], considering that the data has a large number of time steps. To avoid this, the LSTM [54], a type of RNN architecture employed to efficiently learn long-term dependencies in data, is chosen to be implemented.

The LSTM architecture introduces two new concepts to increase its capacity to deal with more time steps: a cell state to capture long-term information and three gates that control the intensity of the data passing through them. The structure of an LSTM cell and all of its additional concepts are represented in Fig. 5.

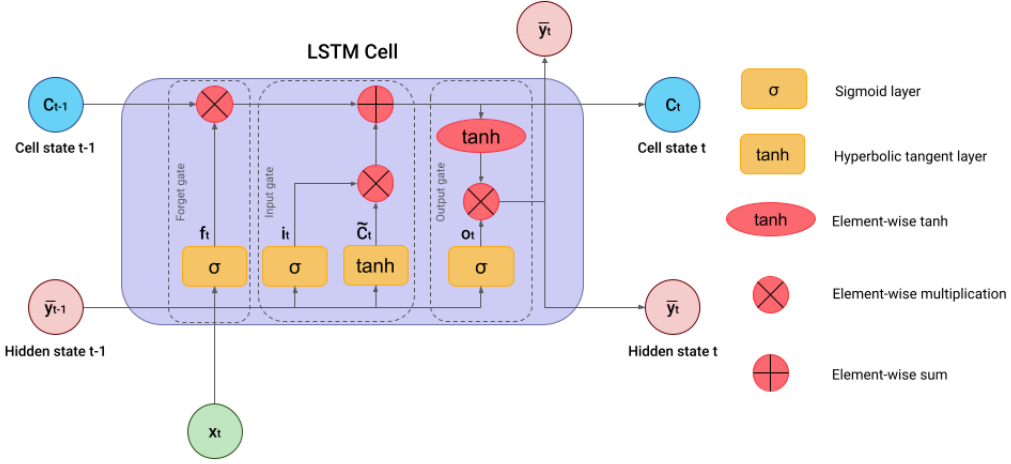


Fig. 5: LSTM Cell structure.

In contrast to the hidden state, which mostly carries information from the previous time step, the cell state is capable of passing data through multiples cells, thanks to its contents suffering only minor reductions and/or increments between each time step.

The gate mechanisms are constructed by a sigmoid neural network layer responsible for transforming a certain input into outputs with values in the range  $[0, 1]$ . These values are called keys, since they are used to tune the data passing through the gates, with 0 erasing the data, 1 passing it integrally and  $]0, 1[$  passing it partially.

The first gate, also known as the forget gate, is responsible for controlling how much each information from the previous cell state  $C_{t-1}$  will pass on to  $C_t$ . Its keys ( $f_t$ ) are defined as

$$f_t = \sigma(W_f \cdot [\bar{y}_{t-1}, x_t] + b_f), \quad (16)$$

where  $\sigma$  is the sigmoid activation function,  $W_f$  is a weight matrix,  $[\bar{y}_{t-1}, x_t]$  is the concatenation of the previous cell's output with the current cell's input and  $b_f$  is a bias.

The second gate, known as the input gate, controls the intensity with which the information obtained from the current cell will be added to the new cell state. The new information candidate  $\tilde{C}_t$  and the keys  $i_t$  that regulate its intensity are defined as follows

$$i_t = \sigma(W_i \cdot [\bar{y}_{t-1}, x_t] + b_i) \quad (17)$$

$$\tilde{C}_t = \tanh(W_C \cdot [\bar{y}_{t-1}, x_t] + b_C), \quad (18)$$

with that, all the mechanisms necessary to define the new cell state  $C_t$  were described. While the forget gate controls how much of the old cell state data will continue to pass, the input gate controls how much of the new information will be added to the cell state. To update it, the expression is defined as

$$C_t = f_t * C_{t-1} + i_t * \tilde{C}_t. \quad (19)$$

The third and final gate, also called the output gate, is responsible for defining how much of the cell state information will be passed to the output  $\bar{y}_t$  of the cell and the hidden state. Before using the information from the cell state, the hyperbolic tangent function is applied to reduce the range of its values. The keys ( $o_t$ ) and the final output of the cell ( $\bar{y}_t$ ) are given by

$$o_t = \sigma(W_o[\bar{y}_{t-1}, x_t] + b_o), \quad (20)$$

$$\bar{y}_t = o_t * \tanh(C_t). \quad (21)$$

Now that the main features of the LSTM architecture and the motivation for using it have been highlighted, the next step is to organize the overall machine learning architecture that will be used to predict certain features.

The most interesting features to predict, whether in a numerical or in an experimental sense, are divided in two types depending on the output type, being static predictions, where each predicted feature has only one value, and transient predictions, where each predicted feature has its values changing through time. Our work focuses on the transient predictions, but an exploration of static predictions is also provided in Section C.2.

For the input, there can be both static and transient features. Since the input dimensions need to be the same for every feature, all of the static data are repeated so that each have multiple time steps with the same value. For example, for the input of the dimensionless number  $Re$ , the repetition would generate  $Re(0) = Re(1) = \dots = Re(t_{max})$ .

For the hidden layers, we have a number of LSTM layers, followed by a Dense layer to generate values within the expected range for predictions and a Reshape layer to control the output shape. The schematics for the input/output relations of one of the explored neural network structures for the droplet collision problem is shown in Fig. 6.

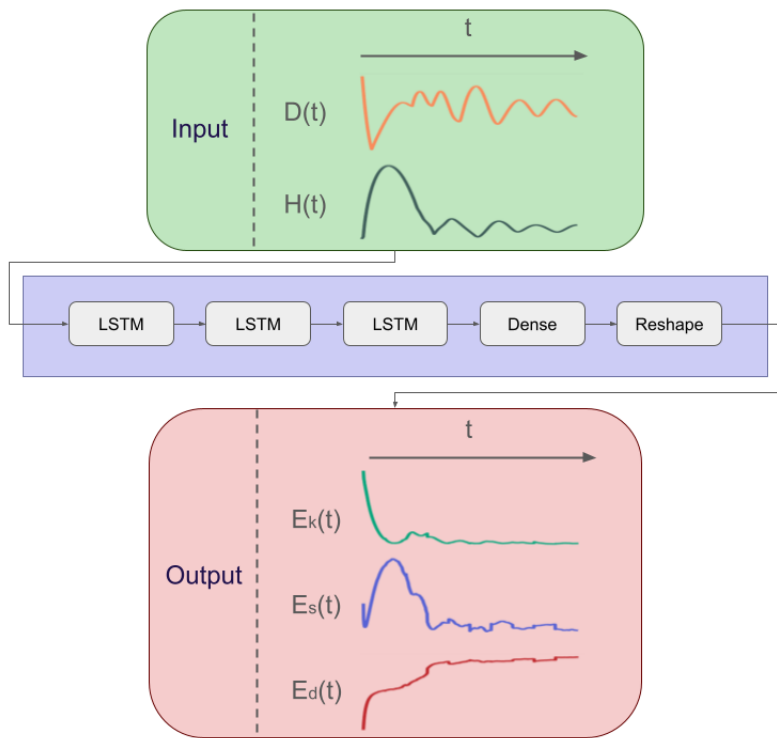


Fig. 6: Machine Learning architecture for transient energy predictions using transient geometric data for the droplet collision problem.

To better visualize the explored predictions, all test cases are shown in Tab. 4, characterized by output type (static or transient), dataset used, input features and output features.

Test cases			
Type	Dataset	Input	Output
Transient	Spreading	$t, D(t), \text{Re}, \text{We}$	$E_k(t), E_s(t), E_d(t)$
Transient	Collision	$D(t), H(t), \text{Re}, \text{We}, \text{B}$	$E_k(t), E_s(t), E_d(t)$
Transient	Collision	$D(t), H(t)$	$E_k(t), E_s(t), E_d(t)$
Static	Collision	$E_k(t), E_s(t), E_d(t)$	$\text{Re}, \text{We}$

Table 4: Description of the explored test cases.

### III. RESULTS

A supervised LSTM network was employed to train models capable of predicting the energy budget based on geometric time series data extracted from numerical simulations. Initially, to test the predictive performance and adaptability of the architecture, two models were trained by using each of the previously defined datasets.

#### A. Performance of the model formulations

Firstly, as the hyperparameter tuning is a crucial stage for applying machine learning modeling, in the current work we have employed the open source hyperparameter optimization framework *Optuna* [55]. After a detailed investigation considering the datasets obtained by the simulations of droplets with varying initial shapes impacting on solid surfaces and collision of droplets, the hyperparameters were chosen as follows

- Learning rate of 0.0001;
- Maximum of 5000 epochs;
- Batch sizes of 8 for spreading and 32 for collision;
- 3 LSTM hidden layers with 32 neurons each;
- 1 Dense output layer with  $n \times m$  neurons, where  $n$  represents the number of time steps and  $m$  represents the number of features;
- 1 Reshape layer (transient output only);
- Adam as an optimization algorithm;
- Mean square error applied as the loss function.

Additionally, an early stopping is applied based on training loss (collision) or validation loss (spreading).

To measure the predictive capability of each model, we used the Coefficient of determination -  $R^2$  (22), the Root Mean Square Error -  $RMSE$  (23) and the Normalized Root Mean Square Error -  $NRMSE$  (24) defined, respectively, as

$$R^2 = 1 - \frac{\sum_{i=1}^N (y_i - \tilde{y}_i)^2}{\sum_{i=1}^N (y_i - \bar{y})^2}, \quad (22)$$

$$RMSE = \sqrt{\frac{1}{N} \sum_{i=1}^N (y_i - \tilde{y}_i)^2}, \quad (23)$$

$$NRMSE = \frac{RMSE}{y_{max} - y_{min}}, \quad (24)$$

where  $N$  is the number of samples,  $y_{max}$  and  $y_{min}$  are, respectively, the maximum and the minimum possible value for the feature,  $y_i$  and  $\tilde{y}_i$  are, respectively, the expected and the predicted value, and  $\bar{y}$  is the average of all expected values.

The  $R^2$  is employed to assess how well the variability of the dependent variables (energies) can be explained by the variability of the independent variables (geometric data and dimensionless numbers). A score approaching 0 indicates a poor explanatory capability, while a score nearing 1 signifies a strong explanatory capability for the dependent variable.  $RMSE$  and  $NRMSE$  are both used to evaluate

the quality of the predictions. While RMSE generates a value dependent on the scale of the predicted variables, NRMSE is used to provide a relative measure of error regardless of the data scale. In both cases, a value close to zero indicates a well-fitted model.

While metrics (22) and (23) are used to individually measure the efficiency of each model, (24) is used to compare models and check the adaptability of the chosen architecture.

For the spreading dataset, 10 different shapes are split into 70% training (7 shapes, 95 samples), 20% validation (2 shapes, 27 samples) and 10% test (1 shape, 10 samples). To optimize the training process, validation loss is used as an early stopping control parameter.

The  $R^2$  score for each individual sample ranges from 0.98315 to 0.9994, while the  $RMSE$  ranges from 0.01122 to 0.05893. Overall, both metrics fall within the expected optimal range and the majority of the predictions fall within a  $\pm 10\%$  error range. Additionally, we observe that these metrics remain rather consistent across all samples, providing further evidence that the model is well-fitted.

For the collision dataset, 72 samples are split into 70% training (50 samples) and 30% test (22 samples). To optimize the training process, training loss is used as an early stopping control parameter.

The  $R^2$  score for each of the 22 test samples ranges from 0.95291 to 0.99997, with the  $RMSE$  ranging from 0.00115 to 0.04618. Given the increased variability in energy behavior, it is understandable how the range of the metrics is larger than in the spreading case. Another contributing factor is that there are less samples in the training dataset with higher Reynolds values, resulting in lower accuracy for predictions within that range.

Despite this difference, both metrics still fall near the optimal ranges, even presenting higher accuracy with fewer training samples than the spreading dataset, as will be shown next. This also shows that predicting the behavior of a new drop shape (spreading case) is more complex than predicting the behavior of new flow parameters (collision case).

Previously, the metrics were analyzed for each sample individually. To assess the overall prediction accuracy of the models, Table 5 compares the error metrics for all training and test samples from both datasets.

Metric	Training samples		Test samples	
	Spreading	Collision	Spreading	Collision
$R^2$	0.9924	0.99996	0.99429	0.99559
$RMSE$	0.03677	0.00124	0.02957	0.0137
$NRMSE$	0.03674	0.0019	0.02961	0.02096

Table 5: Comparison of the evaluation metrics for each dataset.

Since the training datasets are employed in training the model, it is expected that their metrics should also be optimal. Nevertheless, comparing these metrics with those of the test datasets provides insights into how well the model has acquired adaptability to new sets of data that were not used during training.

The most important metric for comparison between both models is the  $NRMSE$ , as it offers a normalized measure of error, disregarding the scale of the data. With these insights, we can infer that the chosen architecture is not only reasonably accurate but also highly versatile for different regimes.

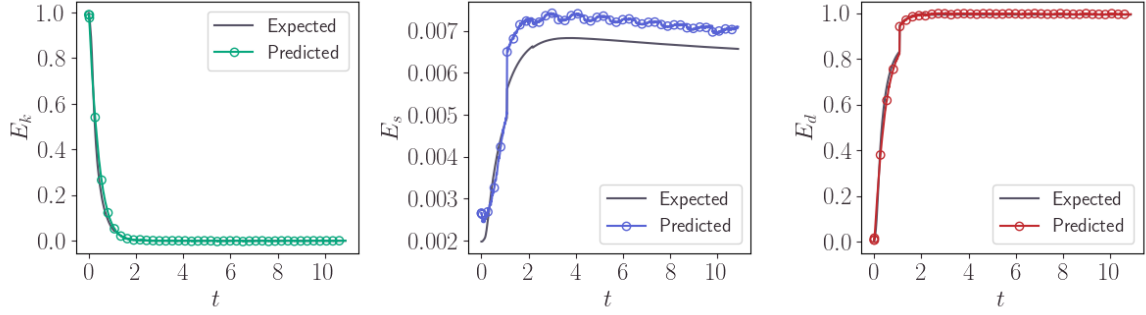
## B. Prediction for the energy budget

To better visualize the model’s efficiency for the spreading case, we first analyse the prediction behavior of two different samples shown in Fig. 7. Each energy plot is normalized by the total energy in the first time step ( $E_t(0)$ ).

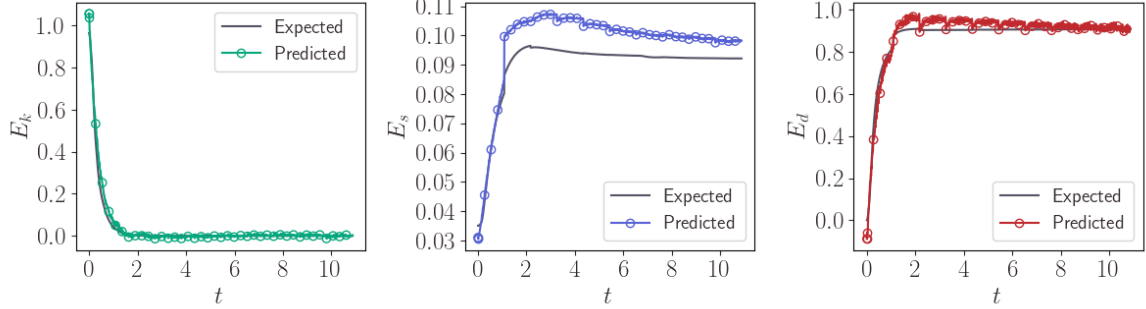
In Figs. 7(a) and 7(b), we can observe pronounced fluctuations caused by the sliding technique (as depicted in Fig. 1) applied to the dataset. Given that each sample is divided into multiple sub-samples, the predictions can oscillate between each one of them, as observed in the surface energy  $E_s$  shown in Fig. 7(a) and the viscous dissipation  $E_d$  from Fig. 7(b). While it may appear to increase errors, some tests have shown that the technique, in fact, enhances model accuracy by generating more samples and using fewer time steps, which reduces training complexity.

Since most samples from the training and test datasets exhibit a lower range of surface energy ( $E_s$ ) values, as illustrated in Fig. 7(a), their prediction errors end up being the most visually accentuated.

The predominance of samples within this lower range also influences the training process. Samples with lower Weber numbers, which have higher surface tension effects, exhibit higher surface energies compared to the majority. As depicted in Fig. 7(b), this higher surface energy undermines accuracy, as



(a) 1st sample -  $Re = 30.73$ ,  $We = 1659.38$ .



(b) 4th sample -  $Re = 24.81$ ,  $We = 90.62$ .

Fig. 7: Comparison between the expected and predicted energy time series from two samples of the spreading test dataset.

the model is primarily tuned for lower values. On the other hand, a higher Reynolds number can impact the prediction of kinetic energy  $E_k$ , affecting the capability of accurately predicting the curve in the few steps leading up to when the drop stops moving, as somewhat depicted in Fig. 7(b).

In general, the main difference in energy behavior observed in the spreading dataset lies in the steepness of its curves. Since the initial drop shape is one of the key factors influencing this behavior, the analysis indicates that the model is capable of generating accurate predictions for samples with a new drop shape (see Fig. 2).

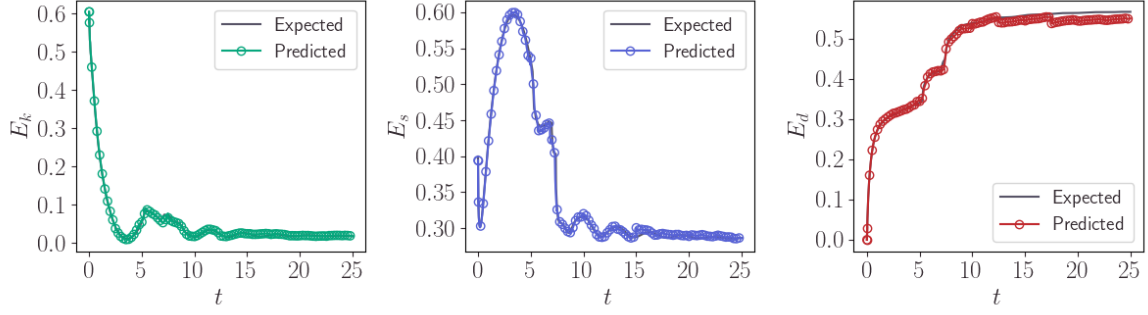
For the collision dataset, we illustrate in Fig. 8 the prediction behavior of two different test cases. Again, the energy plot is normalized using the total energy in the first time step.

The collision adds another layer of complexity to the problem, as the energies now exhibit oscillations over time. In Fig. 8(a) we observe that the model can produce accurate predictions even when there is an anomaly in the curves (as seen at time  $t \approx 6$ ). Furthermore, although fluctuations in viscous dissipation  $E_d$  are still detectable, they occur much less frequently. Decreasing  $Re$  and  $We$ , as illustrated in Fig. 8(b), the coalesced droplet experiences an oscillatory regime that can also be correctly captured by the prediction. Overall, according to these figures, we can confirm the excellent agreement between the expected and predicted results.

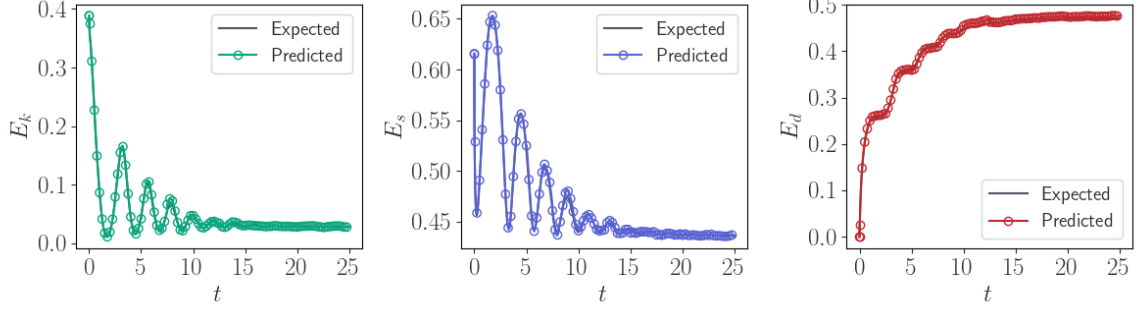
### C. Two-phase prediction with sequential neural networks

To further investigate the significance of our proposed methodology, we adopt a two-phase prediction strategy tailored specifically for the droplet collision problem. Initially, we consider only the drop diameter  $D(t)$  and height  $H(t)$  as inputs to our model. Through this initial phase, our aim is to accurately estimate the energy budget associated with the collision process. Subsequently, leveraging the insights gained from the energy budget prediction, we extend our model to predict static values, such as the nondimensional parameters  $Re$  and  $We$ .

This two-phase prediction approach holds particular relevance in experimental settings where obtaining precise fluid parameters is challenging. Often, despite having access to video data from experiments, the lack of comprehensive knowledge regarding the fluid properties impedes accurate prediction of the energy budget. In such scenarios, our method offers a robust solution by including geometric data to not only predict the energy budget but also estimate essential dimensionless parameters crucial for understanding the underlying physics of droplet dynamics. Using this innovative two-phase prediction process, we bridge the gap between experimental observations and theoretical insights, thereby enhancing our



(a) 1st sample -  $Re = 115.56$ ,  $We = 53.0$ ,  $B = 0.17$ .



(b) 21st sample -  $Re = 74.45$ ,  $We = 22.0$ ,  $B = 0.27$ .

Fig. 8: Comparison between the expected and predicted energy time series from three samples of the collision test dataset.

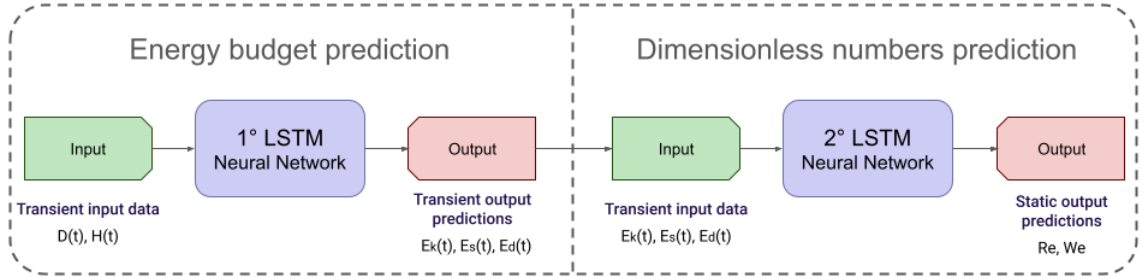


Fig. 9: Two-phase schematics for the energies and dimensionless numbers predictions.

ability to analyze and interpret droplet collision phenomena with greater precision and efficiency.

In summary, this process involves two separate neural networks. The output of the first network, which predicts the energy budget, serves as input for predicting the dimensionless numbers in the second network, as illustrated in Fig. 9.

### C.1 Energy budget prediction

For the first step, we employ an LSTM network to predict all three energies using only the diameter  $D(t)$  and height  $H(t)$  of the droplet. Fig. 10 illustrates an example of how the energy prediction behavior is affected when dimensionless numbers are omitted as inputs.

Although the model experiences a decrease in accuracy when the dimensionless numbers are removed, the overall behavior of the energies is still correctly captured. Moreover, given the extremely limited availability of collectable data from just a video, this increase in error remains tolerable. To assess the differences in metrics across training and test samples for both configurations, let us examine Table 6.



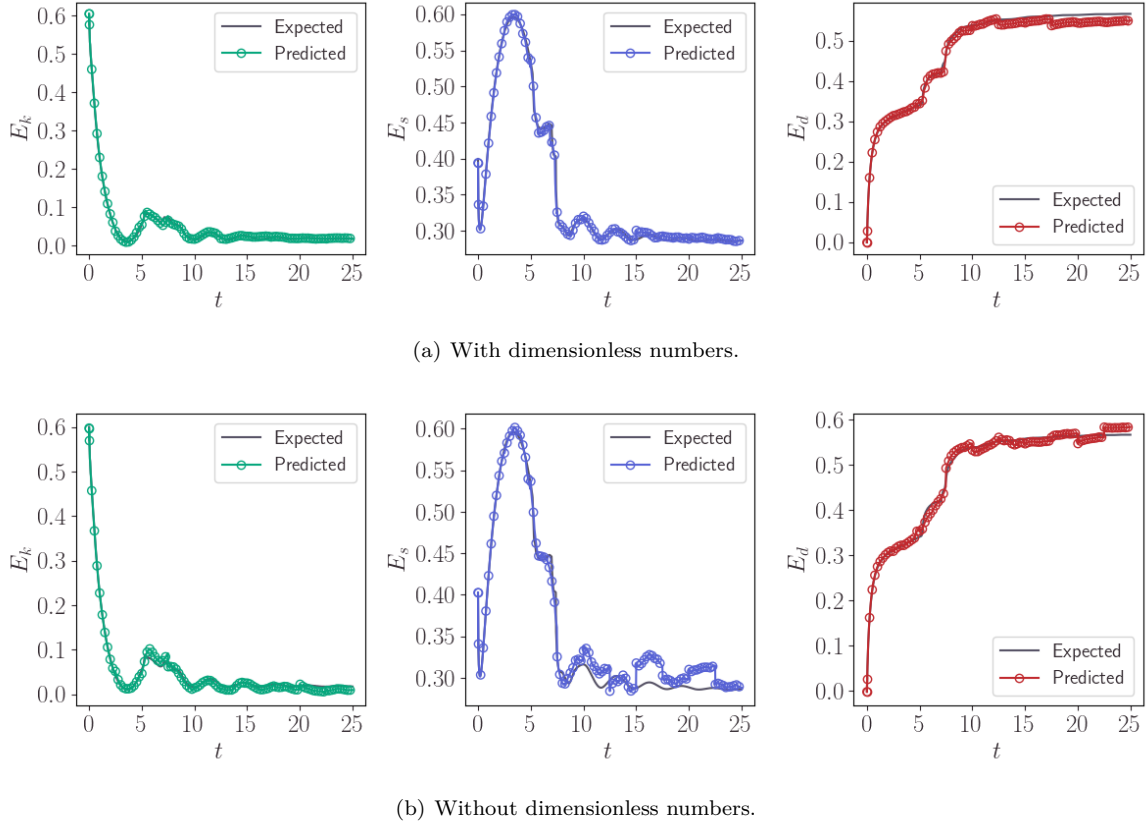


Fig. 10: Comparison between energy predictions with and without the dimensionless numbers as inputs -  $Re = 115.56$ ,  $We = 53.0$ ,  $B = 0.17$ .

Metric	Training samples		Test samples	
	With	Without	With	Without
$R^2$	0.99996	0.99963	0.99604	0.9776
$RMSE$	0.00124	0.00401	0.02732	0.03087
$NRMSE$	0.0019	0.00615	0.02736	0.04725

Table 6: Comparison of the evaluation metrics for models with and without dimensionless numbers  $Re$ ,  $We$  and  $B$  as inputs.

In general, if the dimensionless numbers are known, it is advisable to choose the model that has been trained with them included. However, upon comparing the metrics, it is evident that utilizing only geometric data for the model remains a viable option with decent accuracy.

## C.2 Dimensionless numbers prediction

In a parallel test, we attempted to predict the dimensionless numbers directly using only geometric data. However, this approach resulted in poor prediction accuracy for the collision dataset, as shown in Appendix B.

Therefore, rather than directly using  $D(t)$  and  $H(t)$  to predict the dimensionless numbers  $Re$  and  $We$ , the second step involves utilizing the previously trained neural network to predict the energies and then training a new neural network to predict the dimensionless numbers using these energies.

Given that each sample is divided into 100-time-step slices, the selected prediction for a sample is determined by the median of the predicted values for each of its 10 slices. This is done to mitigate potential noise caused by high errors resulting from using approximated energies as inputs. The prediction results for the collision test dataset are depicted in Fig. 11.

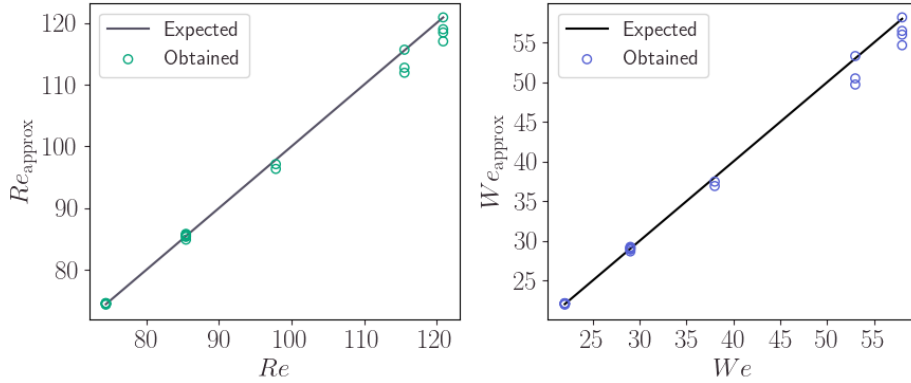


Fig. 11: Dimensionless numbers predictions for each of the 22 samples from the droplet collision test dataset.

Despite the introduction of some noise through the use of approximated energies, the overall predicted values still appear to align with the expected. To quantitatively analyze the results, the previous metrics are calculated both for training and test data in Table 7.

Metric	Training samples	Test samples
$R^2$	0.99366	0.99823
$RMSE$	2.50602	1.39455
$NRMSE$	0.02534	0.0141

Table 7: Comparison of the evaluation metrics for the prediction of the dimensionless numbers by using predicted energies.

With this, we have demonstrated that, in certain regimes, it may be feasible to predict energies and dimensionless numbers using only geometric data extracted from experiment videos. As a follow-up to this study, new architectures could be developed and tested with additional datasets to enhance the neural network generalization, thereby expanding its applicability to a wider range of regimes.

#### IV. CONCLUSIONS

Initially, we proposed two LSTM models to predict the energy balance in two moving free surface problems: the impact of non-spherical droplet in a rigid surface and the collision of two equal-sized droplets. Since the first dataset required generating data from different and unusual shapes, a method capable of extracting particles from interfaces present in digital images was also developed (as shown in Appendix A). Following this test, a two-phase sequential prediction approach was applied in an attempt to predict important properties using exclusively geometric data. This method is specially useful for experimental observations, since it only uses data which can be easily extracted from experiment images or videos. It provides an easy-to-use tool for the challenging task of predicting fluid parameters such as the energies and the dimensionless numbers.

In the context of one-phase prediction, both models shared the same overall architecture, with the only variation being in the data used for training. The first model was trained using data from 95 numerical simulations involving seven different shapes, extracted from images of real experiments, impacting a solid surface and spreading over time. The second model utilized data from 50 numerical simulations of two colliding drops that spread and retracted after coalescence, causing oscillations in the energy budget. For the droplet impact problem, the inputs to the neural network consist of simulation time, the temporal series of the droplet diameter and nondimensional numbers. However, for the droplet collision scenario which is more complex than the spreading case, the model is initialized with the temporal series of diameter and height of the coalesced droplet, in combination with nondimensional numbers and the impact parameter. In both models, the output corresponds to the energy budget.

To evaluate the performance of each model, we conducted a comprehensive metric analysis commonly employed in machine learning modeling, which includes the Coefficient of Determination ( $R^2$ ), the Root Mean Square Error ( $RMSE$ ), and the Normalized Root Mean Square Error ( $NRMSE$ ). The  $R^2$ ,  $RMSE$  and  $NRMSE$  metrics for both models are, respectively, 0.99429 and 0.99559, 0.02957 and 0.0137, and 0.02961 and 0.02096. After analyzing the metrics, we can observe that both models achieved performances

sufficiently close to the ideal values for each metric, with  $R^2s$  close to one and  $RMSEs$  approaching zero. The analyzed models are accurate in a similar way, even when applied to considerably different problems, which can be evaluated by the similarity of their  $NRMSEs$ . The spreading model showed promising results by successfully handling a completely new shape. Similarly, the collision dataset’s model performed well with samples featuring sets of parameters not used during training. The accuracy of the models is also evaluated through plots depicting the kinetic, surface, and viscous dissipation, confirming excellent agreement between the simulation data and the predicted values. This suggests that the machine learning architectures have the potential to be highly adaptable and accurate across a range of fluid regimes.

According to the results for a two-phase prediction, the architecture remains similar, but now follows a two-step scheme. Firstly, an LSTM network predicts the energy budget using only geometric data. Then, the predicted energies serve as inputs in a second LSTM network to predict the static dimensionless numbers. The metrics for the first phase (energies) and the second phase (static prediction for Reynolds and Weber numbers) are, respectively, 0.9776 and 0.99823, 0.03087 and 1.39455, and 0.04725 and 0.0141. Despite a slight increase in error when compared to the one-phase prediction strategy, the metrics for two-phase predictions still demonstrate high accuracy. After the performance investigation concerning the metrics, we have also included the results for predicting the Reynolds and Weber numbers. Results show excellent agreement for low values of Re and We, whereas for larger values, the neural network appears to have more difficulty in establishing accurate predictions. This difficulty can be attributed to the fact that, for the training data, there are fewer instances with higher Re and We values, as seen in Table 3. Finally, this approach proves useful in the sense that directly attempting to predict the dimensionless numbers yielded higher errors, as demonstrated in Appendix B.

While the metrics indicate high versatility, there are still some questions which must be explored. One notable task is the challenge of predicting regimes beyond coalescence in the collision model, given that our current model predominantly relies on coalescence data. For instance, capturing the distinct behaviors associated with the bouncing regime poses a significant challenge, as transitioning between regimes presents a complex task for machine learning models. Future research could be focused on finding new appropriate fluid parameters specific to the bouncing phenomena (or any other regime, for that matter) and exploring interpretation and generalization of the model.

We hope that this research will shed light on the advantages of leveraging the performance offered by LSTM architectures for predicting different types of transient data in complex flows of complex fluids, as for instance dynamics of viscoelastic droplets [56, 57].

## ACKNOWLEDGEMENTS

The authors would also like to thank the financial support given by the São Paulo Research Foundation (FAPESP) grants #2013/07375-0 and #2021/14953-6, the National Council for Scientific and Technological Development (CNPq), grants #305383/2019-1 and CAPES. The authors also acknowledge the Numerical Simulation Laboratory at FCT/UNESP for their support with cluster resources. C.M. Oishi would like to thank the insightful discussions on machine learning modeling held with the research team during his visit at the AI Institute in Dynamic Systems, University of Washington.

# Appendices

## A. DROP SHAPE EXTRACTION FROM AN IMAGE

One of the limitations observed in most flow solvers is that defining interfaces with unusual formats is a difficult process. In the experimental environment, creating spherical or elliptical drops that are strictly symmetrical is a practically impossible task. However, when running numerical simulations to reproduce such experiments, it is often chosen to use these formats because they present parametric equations that easily define them.

In order to be able to define drops with shapes similar to those observed in experiments, thus allowing the testing of network architectures without introducing noise due to shape approximations, a method capable of extracting interfaces present in digital images was also developed in this work. To extract particles from an image, the steps shown on Fig. 12 are performed:

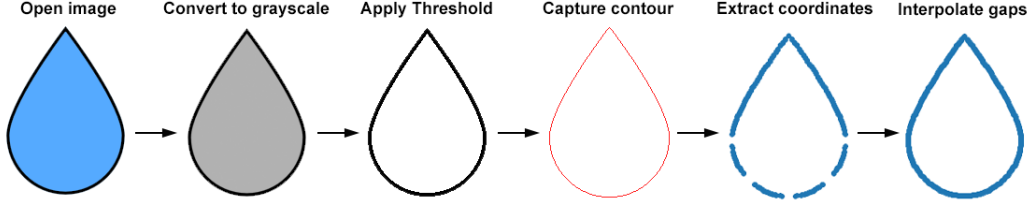


Fig. 12: Steps to extract particles from an image.

- Step 1:** open an image that contains the interface. Preferably, the interface should be outlined with another color to help the contour detection process;
- Step 2:** change the image to grayscale or directly to black and white (recommended only for cases that feature easy-to-extract interfaces with little to no noise);
- Step 3:** for images converted to grayscale, apply a threshold. Based on a threshold value, image pixels are converted to white or black. If a pixel has a value lower than the threshold ( $L$ ), it is changed to black (0). Otherwise, it is changed to white (255). For the example in Fig. 12, a threshold of  $L = 110$  was applied;
- Step 4:** extract the contour(s) of the image that represents the interface(s). In the example previously shown, there is only one continuous interface, so only one contour was detected;
- Step 5:** approximate the contour shape by collecting a set of discretized points  $(i, j)$ . Since the points collected by the function are actually the indices of the pixels from the image's contour, they need to be adjusted so that they fall in the ranges  $[x_{min}, x_{max}]$  and  $[y_{min}, y_{max}]$ :

$$x = \frac{j(x_{min} - x_{max})}{m} + x_{max}$$

$$y = \frac{i(y_{min} - y_{max})}{n} + y_{max}$$

With  $n \times m$  being the dimensions of the input image and  $(x, y)$  being the new coordinates for the points extracted from the interface. As the list of pixels returned is ordered, the method facilitates the creation of particles for representation by front-tracking.

- Step 6:** If the function returns an insufficient number of points or generates points with large spacing (as seen in the previous example), it is possible to apply linear interpolation to create new intermediate points.

To do this, the Euclidean distance between each pair of points is calculated and, if the distance is greater than a chosen maximum tolerance, new intermediate points are generated.

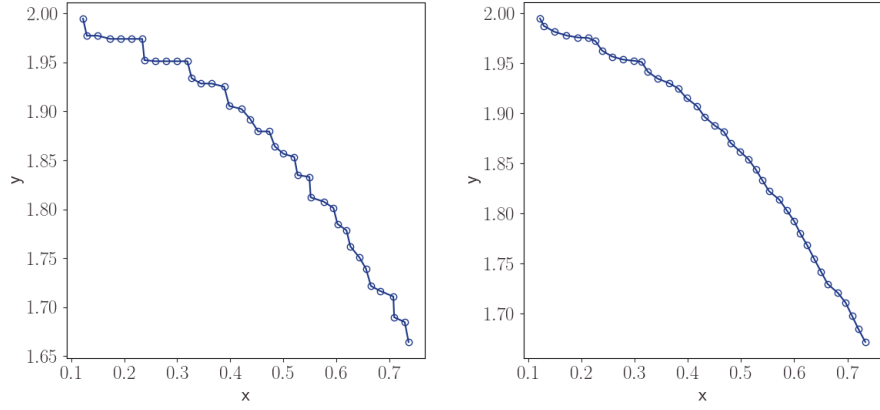
As the method involves extracting points through the pixels of an image's contours, the main restriction observed is that the extraction is limited by the image's resolution. The more pixels an image has, the more accurate the extracted interface will be.

Furthermore, as the points are extracted from the lower left corner of each pixel, aliasing behavior is generated in the extracted points, as can be seen in Fig. 13(a).

This disturbance in the initialization of points can generate atypical behavior in the earlier steps of the simulation. To help solve the aliasing problem, a technique was applied directly to the solver.

The Trapezoidal Sub-grid Undulations Removal (TSUR), developed by [58], is a mass conserving smoothing method used to reduce aliasing and abrupt undulations in curves. The result of applying the method is shown in Fig. 13(b).

In addition to the usefulness of TSUR in removing the initial aliasing of the interface, the technique can also reduce numerical noise that may appear during the simulation, generating more physically accurate approximations.



(a) Aliasing generated when extracting points from pixels. (b) The new points after applying TSUR to reduce aliasing.

Fig. 13: Comparison before and after applying the TSUR technique.

## B. STATIC PREDICTIONS FOR THE DIMENSIONLESS NUMBERS USING GEOMETRIC DATA

To assess the feasibility of predicting dimensionless numbers using only geometric data, we trained an LSTM network using the collision training dataset. Fig. 14 illustrates the predicted values for each instance of the collision test dataset while a detailed metric analysis is presented in Table 8.

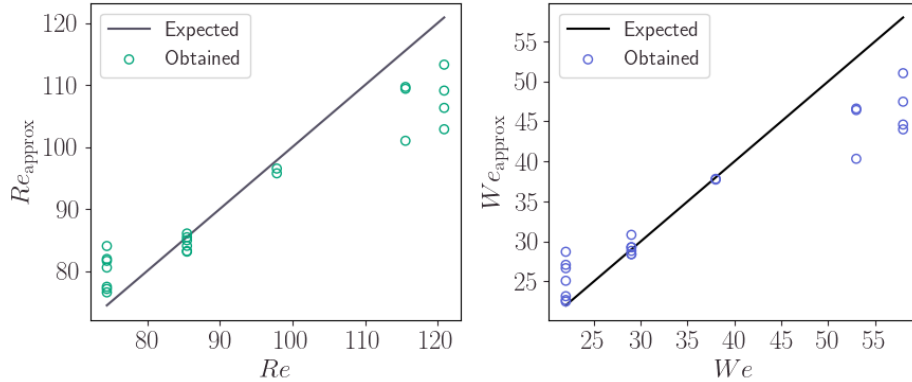


Fig. 14: Direct dimensionless numbers predictions for each of the 22 samples from the collision test dataset.

According to the results in Figs. 11 and 14 and analysing the difference in metrics from Table 8, it is evident that the performance of the one-phase neural network, operating solely on geometrical data as inputs, is inferior to that of our two-stage prediction strategy presented in Section C.2. This comparison highlights the crucial role that is undertaken by the two-phase sequential neural network approach in enhancing the accuracy and robustness of dimensionless number predictions.

Metric	Two-phase	Direct
$R^2$	0.99823	0.95478
$RMSE$	1.39455	7.04277
$NRMSE$	0.0141	0.07122

Table 8: Comparison of the evaluation metrics for the two-phase and direct approaches.

## REFERENCES

- [1] A. L. Yarin, “Drop impact dynamics: splashing, spreading, receding, bouncing. . .”, *Annual Review of Fluid Mechanics* **38**, 159–192 (2006).

- [2] H. A. Stone, “Dynamics of drop deformation and breakup in viscous fluids”, [Annual Review of Fluid Mechanics](#) **26**, 65–102 (1994).
- [3] C. Josserand and S. T. Thoroddsen, “Drop impact on a solid surface”, [Annual Review of Fluid Mechanics](#) **48**, 365–391 (2016).
- [4] S. Lin, B. Zhao, S. Zou, J. Guo, Z. Wei, and L. Chen, “Impact of viscous droplets on different wettable surfaces: impact phenomena, the maximum spreading factor, spreading time and post-impact oscillation”, [Journal of Colloid and Interface Science](#) **516**, 86–97 (2018).
- [5] D. Lohse, “Fundamental fluid dynamics challenges in inkjet printing”, [Annual Review of Fluid Mechanics](#) **54**, 349–382 (2022).
- [6] R. D. Schroll, C. Josserand, S. Zaleski, and W. W. Zhang, “Impact of a viscous liquid drop”, [Phys. Rev. Lett.](#) **104**, 034504 (2010).
- [7] J. Eggers, M. A. Fontelos, C. Josserand, and S. Zaleski, “Drop dynamics after impact on a solid wall: theory and simulations”, [Physics of Fluids](#) **22**, 062101 (2010).
- [8] T. Lee and L. Liu, “Lattice boltzmann simulations of micron-scale drop impact on dry surfaces”, [Journal of Computational Physics](#) **229**, 8045–8063 (2010).
- [9] S. F. Lunkad, V. V. Buwa, and K. Nigam, “Numerical simulations of drop impact and spreading on horizontal and inclined surfaces”, [Chemical Engineering Science](#) **62**, 7214–7224 (2007).
- [10] Y. Pan and K. Suga, “Numerical simulation of binary liquid droplet collision”, [Physics of Fluids](#) **17**, 082105 (2005).
- [11] N. Nikolopoulos, K.-S. Nikas, and G. Bergeles, “A numerical investigation of central binary collision of droplets”, [Computers & Fluids](#) **38**, 1191–1202 (2009).
- [12] I. V. Roisman, “Inertia dominated drop collisions. ii. an analytical solution of the navier–stokes equations for a spreading viscous film”, [Physics of Fluids](#) **21**, 052104 (2009).
- [13] S. Popinet, “An accurate adaptive solver for surface-tension-driven interfacial flows”, [Journal of Computational Physics](#) **228**, 5838–5866 (2009).
- [14] S. Popinet, “Numerical models of surface tension”, [Annual Review of Fluid Mechanics](#) **50**, 49–75 (2018).
- [15] S. Chandra and C. T. Avedisian, “On the collision of a droplet with a solid surface”, [Proceedings of the Royal Society of London. Series A: Mathematical and Physical Sciences](#) **432**, 13–41 (1991).
- [16] N. Laan, K. G. de Bruin, D. Bartolo, C. Josserand, and D. Bonn, “Maximum diameter of impacting liquid droplets”, [Phys. Rev. Appl.](#) **2**, 044018 (2014).
- [17] J. Fukai, Y. Shiiba, T. Yamamoto, O. Miyatake, D. Poulikakos, C. M. Megaridis, and Z. Zhao, “Wetting effects on the spreading of a liquid droplet colliding with a flat surface: experiment and modeling”, [Physics of Fluids](#) **7**, 236–247 (1995).
- [18] J. B. Lee, D. Derome, R. Guyer, and J. Carmeliet, “Modeling the maximum spreading of liquid droplets impacting wetting and nonwetting surfaces”, [Langmuir](#) **32**, 1299–1308 (2016).
- [19] C. Ukiwe and D. Y. Kwok, “On the maximum spreading diameter of impacting droplets on well-prepared solid surfaces”, [Langmuir](#) **21**, 666–673 (2005).
- [20] K.-L. Pan, C. K. Law, and B. Zhou, “Experimental and mechanistic description of merging and bouncing in head-on binary droplet collision”, [Journal of Applied Physics](#) **103**, 064901 (2008).
- [21] J.-P. Estrade, H. Carentz, G. Lavergne, and Y. Biscos, “Experimental investigation of dynamic binary collision of ethanol droplets – a model for droplet coalescence and bouncing”, [International Journal of Heat and Fluid Flow](#) **20**, 486–491 (1999).
- [22] J. Qian and C. K. Law, “Regimes of coalescence and separation in droplet collision”, [Journal of Fluid Mechanics](#) **331**, 59–80 (1997).
- [23] J. Qian, G. Tryggvason, C. Law, J. Qian, G. Tryggvason, and C. Law, *An experimental and computational study of bouncing and deformation in droplet collision* (American Institute of Aeronautics and Astronautics, 1997).
- [24] K. D. Willis and M. E. Orme, “Experiments on the dynamics of droplet collisions in a vacuum”, [Experiments in Fluids](#) **29**, 347–358 (2000).
- [25] S. Wildeman, C. W. Visser, C. Sun, and D. Lohse, “On the spreading of impacting drops”, [Journal of Fluid Mechanics](#) **805**, 636–655 (2016).

- [26] Š. Šikalo, H.-D. Wilhelm, I. V. Roisman, S. Jakirlić, and C. Tropea, “Dynamic contact angle of spreading droplets: experiments and simulations”, *Physics of Fluids* **17**, 062103 (2005).
- [27] P. Attané, F. Girard, and V. Morin, “An energy balance approach of the dynamics of drop impact on a solid surface”, *Physics of Fluids* **19**, 012101 (2007).
- [28] S. Yang, Y. Hou, Y. Shang, and X. Zhong, “Bpnn and cnn-based ai modeling of spreading and icing pattern of a water droplet impact on a supercooled surface”, *AIP Advances* **12**, 045209 (2022).
- [29] M. Tembely, D. C. Vadillo, A. Dolatabadi, and A. Soucemarianadin, “A machine learning approach for predicting the maximum spreading factor of droplets upon impact on surfaces with various wettabilities”, *Processes* **10**, 1141 (2022).
- [30] J. Tang, S. Yu, X. Hou, T. Wu, and H. Liu, “Universal model for predicting maximum spreading of drop impact on a smooth surface developed using boosting machine learning models”, *Industrial & Engineering Chemistry Research* **62**, 15268–15277 (2023).
- [31] L. Au-Yeung and P. A. Tsai, “Predicting impact outcomes and maximum spreading of drop impact on heated nanostructures using machine learning”, *Langmuir* **39**, 18327–18341 (2023).
- [32] E. Heidari, A. Daeichian, M. A. Sobati, and S. Movahedirad, “Prediction of the droplet spreading dynamics on a solid substrate at irregular sampling intervals: nonlinear auto-regressive exogenous artificial neural network approach (narx-ann)”, *Chemical Engineering Research and Design* **156**, 263–272 (2020).
- [33] R. Choudhury, D. M. T. Nasir, D. R. Kaiser, R. Ghimire, D. A. Aliyu, D. B. Sohani, D. J. Atanbori, D. R. Rathaur, and D. R. Mishra, “Uncovering the effect of physical conditions and surface roughness on the maximum spreading factor of impinging droplets using a supervised artificial neural network model”, *Industrial & Engineering Chemistry Research* **62**, 21208–21221 (2023).
- [34] J. Yee, D. Igarashi, S. Miyatake, and Y. Tagawa, “Prediction of the morphological evolution of a splashing drop using an encoder–decoder”, *Machine Learning: Science and Technology* **4**, 025002 (2023).
- [35] J. Yee, A. Yamanaka, and Y. Tagawa, “Image features of a splashing drop on a solid surface extracted using a feedforward neural network”, *Physics of Fluids* **34**, 013317 (2022).
- [36] J. Yee, D. Igarashi, Pradipto, A. Yamanaka, and Y. Tagawa, *Correlation between morphological evolution of splashing drop and exerted impact force revealed by interpretation of explainable artificial intelligence*, 2023.
- [37] H. L. França and C. M. Oishi, “A machine learning strategy for computing interface curvature in front-tracking methods”, *Journal of Computational Physics* **450**, 110860 (2022).
- [38] A. Gaikwad, T. Chang, B. Giera, N. Watkins, S. Mukherjee, A. Pascall, D. Stobbe, and P. Rao, “In-process monitoring and prediction of droplet quality in droplet-on-demand liquid metal jetting additive manufacturing using machine learning”, *Journal of Intelligent Manufacturing* **33**, 2093–2117 (2022).
- [39] M. Pasandideh-Fard, Y. M. Qiao, S. Chandra, and J. Mostaghimi, “Capillary effects during droplet impact on a solid surface”, *Physics of Fluids* **8**, 650–659 (1996).
- [40] N. G. Hadjiconstantinou, “Estimating the maximum splat diameter of a solidifying droplet”, *ASME International Mechanical Engineering Congress and Exposition Heat Transfer: Volume 1*, 311–316 (1999).
- [41] J. B. Lee, D. Derome, A. Dolatabadi, and J. Carmeliet, “Energy budget of liquid drop impact at maximum spreading: numerical simulations and experiments”, *Langmuir* **32**, 1279–1288 (2016).
- [42] L. O. Náraigh and J. Mairal, “Analysis of the spreading radius in droplet impact: the two-dimensional case”, *Physics of Fluids* **35**, 102124 (2023).
- [43] Q. Liu, J. H. Y. Lo, Y. Li, Y. Liu, J. Zhao, and L. Xu, “The role of drop shape in impact and splash”, *Nature communications* **12**, 3068 (2021).
- [44] Z. Zhang and P. Zhang, “Kinetic energy recovery and interface hysteresis of bouncing droplets after inelastic head-on collision”, *Physics of Fluids* **29**, 103306 (2017).
- [45] K. H. Al-Dirawi and A. E. Bayly, “A new model for the bouncing regime boundary in binary droplet collisions”, *Physics of Fluids* **31**, 027105 (2019).
- [46] D. Antonov, N. Shlegel, P. Strizhak, D. Tarlet, and J. Bellettre, “Energy analysis of secondary droplet atomization schemes”, *International Communications in Heat and Mass Transfer* **117**, 104666 (2020).

- [47] A. Riaud, C. Wang, J. Zhou, W. Xu, and Z. Wang, “Hydrodynamic constraints on the energy efficiency of droplet electricity generators”, *Microsystems & Nanoengineering* **7**, 49 (2021).
- [48] O. Ramírez-Soto, V. Sanjay, D. Lohse, J. T. Pham, and D. Vollmer, “Lifting a sessile oil drop from a superamphiphobic surface with an impacting one”, *Science Advances* **34**, eaba4330 (2020).
- [49] S. Hochreiter and J. Schmidhuber, “Long short-term memory”, *Neural Computation* **9**, 1735–1780 (1997).
- [50] A. J. Chorin and J. E. Marsden, *A mathematical introduction to fluid mechanics* (Springer-Verlag, 1979).
- [51] C. M. Oishi, R. L. Thompson, and F. P. Martins, “Transient motions of elasto-viscoplastic thixotropic materials subjected to an imposed stress field and to stress-based free-surface boundary conditions”, *International Journal of Engineering Science* **109**, 165–201 (2016).
- [52] L. C. Jain and L. R. Medsker, 1st (CRC Press, Inc., 1999).
- [53] S.-H. Noh, “Analysis of gradient vanishing of rnns and performance comparison”, *Information* **12**, 11 (2021).
- [54] R. C. Staudemeyer and E. R. Morris, “Understanding lstm – a tutorial into long short-term memory recurrent neural network”, (2019).
- [55] *Optuna - a hyperparameter optimization framework*, <https://optuna.org/>, Accessed: 2024-03-07.
- [56] C. M. Oishi, R. L. Thompson, and F. P. Martins, “Impact of capillary drops of complex fluids on a solid surface”, *Physics of Fluids* **31**, 123109 (2019).
- [57] H. L. França and C. M. Oishi, “Numerical investigation of shear-thinning and viscoelastic binary droplet collision”, *Journal of Non-Newtonian Fluid Mechanics* **302**, 104750 (2022).
- [58] L. Nonato, N. Mangiavacchi, F. S. Sousa, A. Castelo, and J. Cuminato, “A mass-conserving smooth method”, *Mecánica Computacional* **23**, 1897–1910 (2004).